THE JOURNAL OF PHYSICAL CHEMISTRY LETTERS
A JOURNAL OF THE AMERICAN CHEMICAL SOCIETY

pubs.acs.org/JPCL

Letter

Quantum Interferometric Pathway Selectivity in Difference-Frequency-Generation Spectroscopy

Hari Kumar Yadalam,* Matthias Kizmann, Jérémy R. Rouxel, Yeonsig Nam, Vladimir Y. Chernyak, and Shaul Mukamel*

Cite This: J. Phys. Chem. Lett. 2023, 14, 10803−10809

Read Online

ACCESS | Metrics & More | Article Recommendations | Supporting Information

ABSTRACT: Even-order spectroscopies such as sum-frequency generation (SFG) and difference-frequency generation (DFG) can serve as direct probes of molecular chirality. Such signals are usually given by the sum of several interaction pathways that carry different information about matter. Here we focus on DFG, involving impulsive optical−optical−IR interactions, where the last IR pulse probes vibrational transitions in the ground or excited electronic state manifolds, depending on the interaction pathway. Spectroscopy with classical light can use phase matching to select the two pathways. In this theoretical study, we propose a novel quantum interferometric protocol that uses entangled photons to isolate individual pathways. This additional selectivity originates from engineering the state of light using a Zou−Wang−Mandel interferometer combined with coincidence detection.

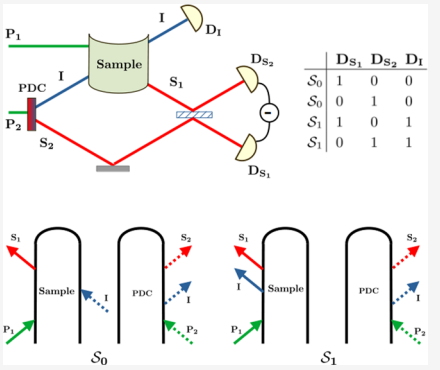

By symmetry, second-order spectroscopic signals $\chi^{(2)}$ vanish in centrosymmetric media.[1−5] As such, they provide sensitive probes of interfaces and of ensembles of randomly oriented chiral molecules,[6−9] in the gas or liquid phase. Sum- and difference-frequency generation (SFG and DFG, respectively) are widely used as chiral-sensitive signals. Time-domain SFG with an infrared pump and an optical probe is commonly used to probe vibrational frequencies and dephasing rates. Controlling the pulse time ordering and the signal direction (phase matching) can generally select groups of relevant pathways but not a single pathway.[10,11] DFG, for example, has two pathways (shown in Figure 3),[12,13] which represent different vibrational transitions in the ground or the excited states. The ability to select a single pathway could simplify the interpretation of signals.

Quantum light provides additional control knobs compared to classical light.[14−18] Entangled photons have been shown to allow better joint spectral-temporal resolution not subjected to the Fourier uncertainty.[19] They further allow carrying out nonlinear spectroscopies at low intensities, making them suitable for studying fragile biological samples.[20−25] Several multidimensional spectroscopy techniques based on entangled photons have been proposed.[26−28]

In this theoretical study, we propose a novel interferometer setup with quantum light, see Figure 1, which can select a single pathway (rather than two) in DFG. This allows better resolution of vibrational transitions in the ground and excited electronic states. Multiphoton interferometers and coincidence counting techniques are commonly used in quantum optics[29−31] and have been proposed to improve the spectral and temporal resolutions in spectroscopy.[32−37]

Recently we have demonstrated pathway selectivity in third order double-quantum-coherence signals.[38] Pathway selectivity in a Raman process without interferometry was discussed in ref. 39. Here we show how to select pathways in DFG using photon-number-resolved detectors in an interferometeric setup.

The proposed setup, depicted in Figure 1, is inspired by the Zou−Wang−Mandel interferometer[40−42] which uses two nonlinear crystals. Recently the Zou−Wang−Mandel interferometer was used for performing imaging[43] and spectroscopy[44,45] with undetected photons.

A single-photon pulse propagating along the optical path $\mathbf{P}$ with polarization ($\boldsymbol{\epsilon}_p$) is split by a beam splitter, into a superposition of two single photon pulses, $\mathbf{P}_1$ and $\mathbf{P}_2$, with the same polarization and a controlled time delay $\delta\tau_p$. $\mathbf{P}_2$ is further split using a nonlinear crystal by undergoing a spontaneous parametric down conversion process, into an entangled photon pair $\mathbf{S}_2$ and $\mathbf{I}$, with respective polarizations $\boldsymbol{\epsilon}_s$ and $\boldsymbol{\epsilon}_i$ and a second controlled time delay $\delta\tau_{si}$. The state of light is then given by a superposition of a single photon pulse $\mathbf{P}_1$ and entangled single photon pulses $\mathbf{I}$ and $\mathbf{S}_2$,

Received: August 21, 2023
Revised: October 18, 2023
Accepted: October 19, 2023
Published: November 28, 2023

https://doi.org/10.1021/acs.jpclett.3c02341
J. Phys. Chem. Lett. 2023, 14, 10803−10809

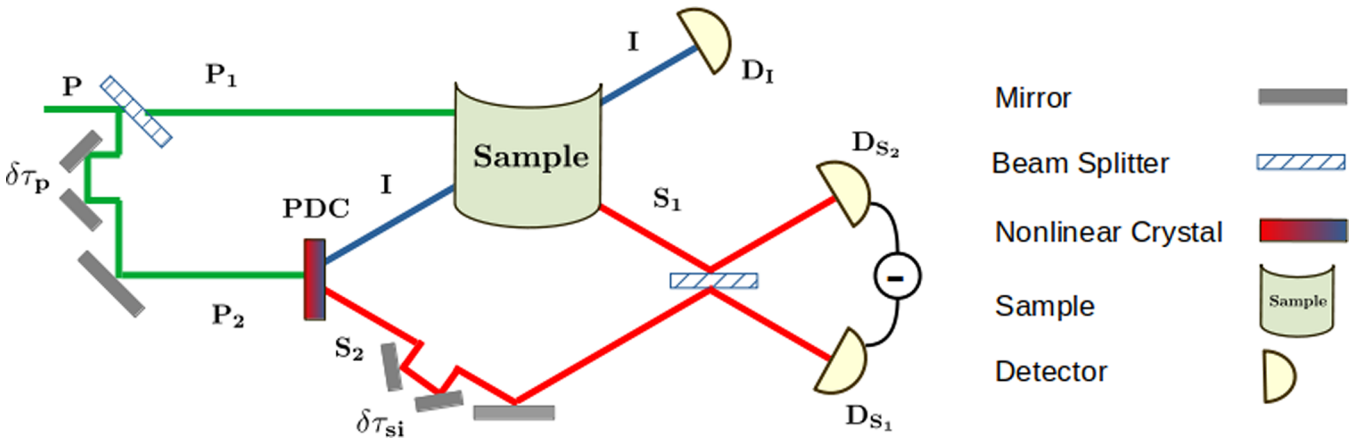

Figure 1. Proposed Zou−Wang−Mandel interferometer for selecting Liouville space pathways in ultrafast DFG spectroscopy. Engineered state of photons along with coincidence detection of photons at the three detectors provides a route for this selectivity.

$$|\Psi(-\infty)\rangle = \frac{1}{\sqrt{2}}[\int_{-\infty}^{+\infty} d\omega_p \phi(\omega_p) a^{\dagger}_{p_1\epsilon_p}(\omega_p) + \int_{-\infty}^{+\infty} d\omega_s d\omega_i \psi(\omega_s, \omega_i) e^{i\omega_s(\delta\tau_p+\delta\tau_{si})+i\omega_i\delta\tau_p} a^{\dagger}_{s_2\epsilon_s}(\omega_s) a^{\dagger}_{i\epsilon_i}(\omega_i)]|\varnothing\rangle \quad (1)$$

where $|\varnothing\rangle$ is the vacuum state of the electromagnetic field and $a_{\alpha\epsilon}(\omega)$ is the bosonic annihilation operator of a photon with frequency ω and polarization ϵ propagating along the optical path α. In the present application, pulses $\mathbf{P_1}$ and $\mathbf{I}$ are in the ultraviolet range and $\mathbf{S_2}$ is infrared. More details are given in the appendix.

Pulses $\mathbf{P_1}$ and $\mathbf{I}$ then interact with the sample to generate a third pulse $\mathbf{S_1}$ via a DFG process. This is ensured by (i) the phase matching condition at the **nonlinear crystal** (**PDC**), $\boldsymbol{k}_{S_2} = \boldsymbol{k}_{P_2} - \boldsymbol{k}_I$, and at the **Sample**, $\boldsymbol{k}_{S_1} = \boldsymbol{k}_{P_1} - \boldsymbol{k}_I$, together with selecting the signals along $\boldsymbol{k}_{S_2}$ and $\boldsymbol{k}_{S_1}$, ensures that the idlers direction is identical, $\boldsymbol{k}_I$, and (ii) pulses $\mathbf{P_1}$ and $\mathbf{I}$, which pass through the sample have a photon in one of them, but not in both (as can be seen from eq 1), and hence do not allow an SFG process.

Finally, a coincidence measurement which includes (i) photon number resolved detection of pulse $\mathbf{I}$ at the detector $\mathbf{D_I}$ and (ii) difference of intensities recorded at the detectors $\mathbf{D}_{S_1}$ and $\mathbf{D}_{S_2}$, which measures coherence (heterodyne) of photons in pulses $\mathbf{S_1}$ and $\mathbf{S_2}$, respectively, generated at the sample and crystal. Our signal is finally defined by $\langle I_{D_I}(n_i)(I_{D_{S1}} - I_{D_{S2}})\rangle$. This coincidence detection, as will be shown below, selectively isolates each Liouville space pathway in Figure 3, based on the photon number in pulse $\mathbf{I}$.

We consider a molecular model system, Figure 2, with two electronic states and their vibrational manifolds. The total matter and field Hamiltonian are given by

$$H = \underset{\text{system}}{H_s} + \underset{\text{field}}{H_f} + \underset{\text{system-field}}{H_{sf}} \quad (2)$$

$$H_s = \sum_{\sigma=g,e}\sum_{n\in\sigma} \hbar\omega_{\sigma_n}|\sigma_n\rangle\langle\sigma_n| \quad (3)$$

$$H_f = \sum_{\alpha\in\mathcal{I}}\sum_{\lambda}\int_{-\infty}^{+\infty} d\omega \hbar\omega a^{\dagger}_{\alpha\epsilon_\lambda}(\omega) a_{\alpha\epsilon_\lambda}(\omega) \quad (4)$$

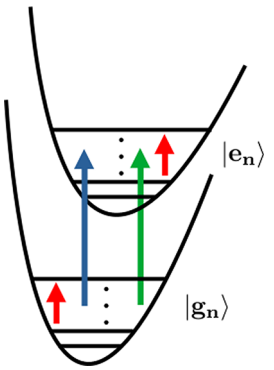

Figure 2. Energy level scheme for a molecular model system consisting of two electronic states (labeled as g and e) each having its own vibrational manifold (labeled by the subscripts g_n and e_n). Optical transitions are the intermanifold vibronic transitions and intramanifold vibrational transitions.

$$H_{sf} = \sum_{\alpha\in p_1,s_1,i} [\mathcal{E}^{\dagger}_{\alpha}\cdot\boldsymbol{V} + \boldsymbol{V}^{\dagger}\cdot\mathcal{E}_{\alpha}] \quad (5)$$

where $\mathcal{I} = p, p_1, p_2, s_1, s_2, i$ indicates a sum over all optical paths in the interferometer. $|\sigma_n\rangle$ denotes the n^{th} vibrational state in the $\sigma = g, e$ manifold. The electric field operator is given by $\mathcal{E}_\alpha = ic_\alpha\sum_\lambda \epsilon_\lambda \int_{-\infty}^{+\infty} d\omega a_{\alpha\epsilon_\lambda}(\omega)$, with $c_\alpha = \sqrt{\frac{\hbar\bar{\omega}_\alpha}{4\pi\epsilon_0 cA}}$. A is the transverse area and $\bar{\omega}_\alpha$ is the central frequency of the pulse along path α. The transition dipole operator is given by

$$\boldsymbol{V} = \sum_{\substack{\sigma,\sigma' \\ \omega_{\sigma_n}<\omega_{\sigma'_{n'}}}} \sum_{n\in\sigma, n'\in\sigma'} \boldsymbol{\mu}_{\sigma_n\sigma'_{n'}} |\sigma_n\rangle\langle\sigma'_{n'}|$$

In the above, the light−matter interaction is given in the rotating-wave approximation.

The coincidence detection of n_i idler photons with heterodyne detection of $\mathbf{S_1}$ and $\mathbf{S_2}$, S_{n_i}, is, for $n_i = 0$

$$S_0 = \frac{1}{\pi c_{s1} c_{s2}} \mathrm{Im}\int_{-\infty}^{+\infty} dt_s dt_i \left\langle \mathcal{T}\mathcal{E}^{\dagger}_{s_2R}(t_s)\cdot\mathcal{E}_{s_1L}(t_s) \left[\delta(t_i) - \frac{1}{2\pi c_i^2}\mathcal{E}^{\dagger}_{iR}(t_i)\cdot\mathcal{E}_{iL}(t_i)\right]\right\rangle \quad (6)$$

https://doi.org/10.1021/acs.jpclett.3c02341
J. Phys. Chem. Lett. 2023, 14, 10803−10809

and for $n_i = 1$

$$\mathcal{S}_1 = \frac{1}{2\pi^2 c_{s1} c_{s2} c_i^2} \mathrm{Im} \int_{-\infty}^{+\infty} \mathrm{d}t_s \mathrm{d}t_i \langle \mathcal{T} \mathcal{E}_{s_2 R}^{\dagger}(t_s) \cdot \mathcal{E}_{s_1 L}(t_s) \mathcal{E}_{iR}^{\dagger}(t_i) \cdot \mathcal{E}_{iL}(t_i) \rangle \tag{7}$$

where $O(t)$ is an interaction-picture operator. The subscripts L, R are superoperator indices representing the action of the operator on the left (ket) or right (bra). Furthermore, $\langle \mathcal{T} \cdots \rangle = \mathrm{Tr}[\mathcal{T} \cdots e^{-(i/\hbar)\int_{-\infty}^{\infty} \mathrm{d}t H_{sf-}(t)} \rho(-\infty)]$, $\rho(-\infty) = |g_1\rangle\langle g_1| \otimes |\Psi(-\infty)\rangle\langle\Psi(-\infty)|$ is the joint initial density matrix of the system and the field. Here $|g_1\rangle$ denotes the ground vibrational state of the ground electronic manifold of the system.

The motivation for the coincidence signals is as follows: When the signals are recorded, only two possible pathways of the light−matter interaction are possible, as represented by the loop diagrams in Figure 3. Figure 3 ($\mathcal{S}_0$) corresponds to a photon in pulse $\mathbf{P}_1$ and a photon in pulse $\mathbf{I}$ being absorbed by the system on the left (ket) and right (bra) side of the joint matter-field density matrix, followed by $\mathbf{S}_1$ photon emission. This results in no final photon in pulse $\mathbf{I}$ and a coherence between photons in pulses $\mathbf{S}_1$ and $\mathbf{S}_2$, which contributes to the signal $\mathcal{S}_0$. This leads to two possible photon count scenarios in the three detectors given in the first two columns of Table 1. Hence, $\mathcal{S}_0$, which measures coherence between $\mathbf{S}_1$ and $\mathbf{S}_2$ combined with zero photons in $\mathbf{I}$, selects Figure 3 ($\mathcal{S}_0$). For diagram Figure 3 ($\mathcal{S}_1$), a photon from pulse $\mathbf{P}_1$ is absorbed by the system on the left side, followed by sequential emission of photons along $\mathbf{I}$ and $\mathbf{S}_1$ on the left side. This results in a single photon in pulse $\mathbf{I}$ and coherence between photons in pulses $\mathbf{S}_1$ and $\mathbf{S}_2$, which contributes to the signal $\mathcal{S}_1$.

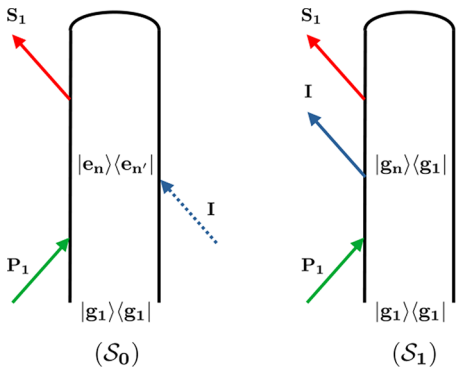

Figure 3. Loop diagrams contribute to the signals. The classical ultrafast DFG signal, $\mathcal{S}^{(c)}$, is given by the sum of both diagrams.

Table 1. Possible Photon Counts at the Detectors for Different Pathways Selected by the Interferometric Signals[a]

	$\mathbf{D}_{\mathbf{S}_1}$	$\mathbf{D}_{\mathbf{S}_2}$	$\mathbf{D}_{\mathbf{I}}$
$\mathcal{S}_0$	1	0	0
$\mathcal{S}_0$	0	1	0
$\mathcal{S}_1$	1	0	1
$\mathcal{S}_1$	0	1	1

[a]The final photon distribution of pulse $\mathbf{I}$, conditioned on a single photon in either of the pulses $\mathbf{S}_1$ or $\mathbf{S}_2$, distinguishes between different Liouville space pathways. Null/one photon count in pulse $\mathbf{I}$ selects Figure 3 ($\mathcal{S}_0/\mathcal{S}_1$).

This leads to two possible photon count scenarios at the three detectors given in the last two columns of Table 1. Hence, $\mathcal{S}_1$, which measures coherence between $\mathbf{S}_1$ and $\mathbf{S}_2$ in coincidence with a photon in $\mathbf{I}$, selects the loop diagram in Figure 3 ($\mathcal{S}_1$). Thus, the proposed coincidence signals can selectively measure the two loop diagrams in Figure 3. Both diagrams in Figure 3 satisfy the same phase-matching condition $\boldsymbol{k}_{\mathbf{S}_1} = \boldsymbol{k}_{\mathbf{P}_1} - \boldsymbol{k}_{\mathbf{I}}$ and hence cannot be separated by a classical DFG measurement which only measures $\mathbf{S}_1$. However, they differ in the final state of the $\mathbf{I}$ field, which is measured in the interferometric measurement. Measuring more than one (as opposed to a single field in a classical measurement) is the key for the pathway selectivity. More additional details are given in the Supporting Information.

Below we present expressions for these signals in terms of system and field multipoint correlation functions. Sum-over-states expressions for the signals are derived as well.

Expanding eqs 6 and 7 to third order in the light−matter coupling and using eq 1 gives

$$\mathcal{S}_0(\bar{\omega}_p, \delta\tau_{si}) = -\mathrm{Im}\left(-\frac{i}{\hbar}\right)^3 \sum_{l,m,n=x,y,z} \int_{-\infty}^{+\infty} \mathrm{d}t_1 \mathrm{d}t_2 \mathrm{d}t_3 \langle \mathcal{T} V_L^l(t_1) V_R^m(t_2) V_L^{n\dagger}(t_3) \rangle_s \langle \mathcal{T} \mathcal{E}_{s_2 L}^{l\dagger}(t_1) \mathcal{E}_{iR}^{m\dagger}(t_2) \mathcal{E}_{p_1 L}^{n}(t_3) \rangle_f \tag{8}$$

and

$$\mathcal{S}_1(\bar{\omega}_p, \delta\tau_{si}) = \mathrm{Im}\left(-\frac{i}{\hbar}\right)^3 \sum_{l,m,n=x,y,z} \int_{-\infty}^{+\infty} \mathrm{d}t_1 \mathrm{d}t_2 \mathrm{d}t_3 \langle \mathcal{T} V_L^l(t_1) V_L^m(t_2) V_L^{n\dagger}(t_3) \rangle_s \langle \mathcal{T} \mathcal{E}_{s_2 L}^{l\dagger}(t_1) \mathcal{E}_{iL}^{m\dagger}(t_2) \mathcal{E}_{p_1 L}^{n}(t_3) \rangle_f \tag{9}$$

The signals $\mathcal{S}_0$ and $\mathcal{S}_1$ depend on the following control parameters: the pulses central frequencies ($\bar{\omega}_{p_1/s_2/i}$), their widths, and the time delays ($\delta\tau_p$ and $\delta\tau_{si}$) between the pulses $\mathbf{P}_1$, $\mathbf{S}_2$, and $\mathbf{I}$. They also depend on the entanglement time of pulses $\mathbf{S}_2$ and $\mathbf{I}$. In the above equations and in the following, we only indicate explicit dependence on $\bar{\omega}_p$ and $\delta\tau_{si}$, which are scanned to obtain the spectral information on the system, while all the other parameters are held constant. We note that, due to the quantum nature of the electromagnetic field interacting with the sample, the above signals cannot be solely expressed in terms of the classical causal response function of matter.[46] Since the signals $\mathcal{S}_0$ and $\mathcal{S}_1$ are obtained using an engineered quantum state of light and a quantum interferometer, we refer to them as the quantum signals in the following.

$$\langle \mathcal{T} V_L^l(t_1) V_{L/R}^m(t_2) V_L^{n\dagger}(t_3) \rangle_s$$

and

$$\langle \mathcal{T} \mathcal{E}_{s_2 L}^{l\ \dagger}(t_1) \mathcal{E}_{iL/R}^{m\ \dagger}(t_2) \mathcal{E}_{p_1 L}^{n}(t_3) \rangle_f$$

are respectively the system and field multipoint correlation functions. The system and field correlation functions are computed with their respective initial states $|g_1\rangle\langle g_1|$ and $|\Psi(-\infty)\rangle\langle\Psi(-\infty)|$, with $|\Psi(-\infty)\rangle$ given in eq 1. The system and field operators evolve according to their respective Hamiltonians given in eq 2.

These signals are represented by the loop diagrams in Figure 3. These loop diagrams are time ordered in loop time and not the real time.[47,48] Depending on the relative time ordering of left and right operators, each loop diagram represents one or more ladder diagrams that are completely time ordered. The loop diagram in Figure 3 ($\mathcal{S}_0$), contributing to $\mathcal{S}_0$, is represented by

https://doi.org/10.1021/acs.jpclett.3c02341
J. Phys. Chem. Lett. 2023, 14, 10803−10809

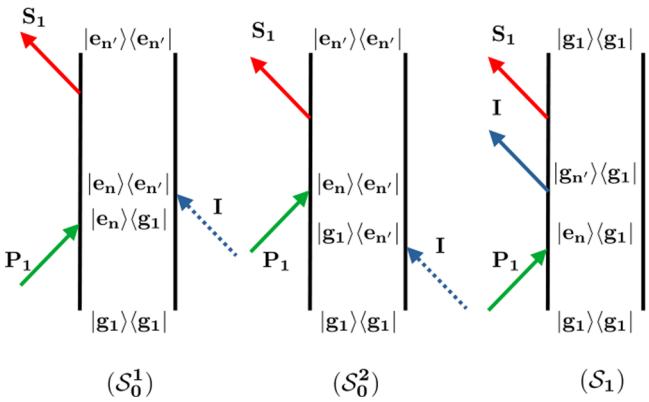

Figure 4. Ladder diagrams corresponding to the loop diagrams of Figure 3. Diagrams $(\mathcal{S}_0^1)$ and $(\mathcal{S}_0^2)$ contribute to $\mathcal{S}_0$, and diagram $(\mathcal{S}_1)$ contributes to $\mathcal{S}_1$. The classical ultrafast DFG signal is given by the sum of all diagrams.

the two ladder diagrams of Figures 4 $(\mathcal{S}_0^1)$ and 4 $(\mathcal{S}_0^2)$, whereas the loop diagram in Figure 3 $(\mathcal{S}_1)$, contributing to $\mathcal{S}_1$, is represented by a single ladder diagram in Figure 4 $(\mathcal{S}_1)$. We assumed that the entangled photons in pulses $\mathbf{S}_2$ and $\mathbf{I}$ are time ordered such that $\mathbf{I}$ comes first. Moreover, in Figure 4, we assumed that pulses $\mathbf{P}_1$ and $\mathbf{I}$ are resonant with interband transitions, whereas $\mathbf{S}_1$ is resonant with intraband transitions.

The two pathways shown in Figure 3, involving ground or excited state vibrational transitions,[12] can thus be sorted out, based on the number of detected photons in the idler pathway. The diagram in Figure 3 $(\mathcal{S}_0)$ describes the signal originating from excited state vibrational coherence, while Figure 3 $(\mathcal{S}_1)$ corresponds to ground state vibrational coherence. The present selectivity in probing these two pathways could find applications in probing excited states of chiral molecules in the bulk and at chiral interfaces.

For an ensemble of randomly oriented molecules, the bulk macroscopic signal can be obtained from the above single molecule signal by averaging over molecular orientations.[49] We note that the rotationally averaged signals vanish for achiral molecules and hence selectively probe chirality. The rotationally averaged quantum signals are finally given by,

$$\mathcal{S}_0(\bar{\omega}_p, \delta\tau_{si}) = -\frac{1}{3!}\mathrm{Im}\left(-\frac{i}{\hbar}\right)^3 \int_{-\infty}^{+\infty} \mathrm{d}t_1\mathrm{d}t_2\mathrm{d}t_3 \langle \mathcal{T}\boldsymbol{V}_L(t_1) \times \boldsymbol{V}_R(t_2)\cdot\boldsymbol{V}_L^{\dagger}(t_3)\rangle_s \langle \mathcal{T}\boldsymbol{\mathcal{E}}_{s_2L}^{\dagger}(t_1) \times \boldsymbol{\mathcal{E}}_{iR}^{\dagger}(t_2)\cdot\boldsymbol{\mathcal{E}}_{p_1L}(t_3)\rangle_f \tag{10}$$

and

$$\mathcal{S}_1(\bar{\omega}_p, \delta\tau_{si}) = \frac{1}{3!}\mathrm{Im}\left(-\frac{i}{\hbar}\right)^3 \int_{-\infty}^{+\infty} \mathrm{d}t_1\mathrm{d}t_2\mathrm{d}t_3 \langle \mathcal{T}\boldsymbol{V}_L(t_1) \times \boldsymbol{V}_L(t_2)\cdot\boldsymbol{V}_L^{\dagger}(t_3)\rangle_s \langle \mathcal{T}\boldsymbol{\mathcal{E}}_{s_2L}^{\dagger}(t_1) \times \boldsymbol{\mathcal{E}}_{iL}^{\dagger}(t_2)\cdot\boldsymbol{\mathcal{E}}_{p_1L}(t_3)\rangle_f \tag{11}$$

Equations 10 and 11 are the main results of this work. We compare them with the classical heterodyne detected DFG signal generated by three temporally separated classical pulses, $\tilde{\boldsymbol{E}}_s(t)$, $\tilde{\boldsymbol{E}}_i(t)$ and $\tilde{\boldsymbol{E}}_p(t)$,

$$\mathcal{S}^{(c)}(\bar{\omega}_p, \delta\tau_{si}) = \frac{2}{3!}\mathrm{Im}\left(-\frac{i}{\hbar}\right)^3 \int_{-\infty}^{+\infty} \mathrm{d}t_1\mathrm{d}t_2\mathrm{d}t_3 \tilde{\boldsymbol{E}}_s^*(t_1) \times \tilde{\boldsymbol{E}}_i^*(t_2)\cdot\tilde{\boldsymbol{E}}_p(t_3) [\langle \mathcal{T}\boldsymbol{V}_L(t_1) \times \boldsymbol{V}_L(t_2)\cdot\boldsymbol{V}_L^{\dagger}(t_3)\rangle_s - \langle \mathcal{T}\boldsymbol{V}_L(t_1) \times \boldsymbol{V}_R(t_2)\cdot\boldsymbol{V}_L^{\dagger}(t_3)\rangle_s] \tag{12}$$

Details of this classical signal are given in the Supporting Information.

By comparing the quantum signals (eqs 10 and 11) with the classical signal (eq 12), it is clear that the quantum signals can selectively probe each of the two contributions to the classical signal. As can be seen from Figure 4, the signals $\mathcal{S}_0$ and $\mathcal{S}_1$ probe excited state and ground state vibrational coherences, respectively. This separation is not possible with the classical signal.

For the state of light given in eq 1, the field correlation functions factorize as

$$\begin{aligned}&\langle \mathcal{T}\boldsymbol{\mathcal{E}}_{s_2L}^{\dagger}(t_1) \times \boldsymbol{\mathcal{E}}_{iL/R}^{\dagger}(t_2)\cdot\boldsymbol{\mathcal{E}}_{p_1L}(t_3)\rangle_f \\ &= \langle \Psi(-\infty)|\mathcal{T}\boldsymbol{\mathcal{E}}_{s_2}^{\dagger}(t_1) \times \boldsymbol{\mathcal{E}}_i^{\dagger}(t_2)|\varnothing\rangle\cdot\langle\varnothing|\boldsymbol{\mathcal{E}}_{p_1}(t_3)|\Psi(-\infty)\rangle \\ &= (2\pi i)^3 c_{s_2}c_{p_1}c_i\boldsymbol{\epsilon}_s^* \times \boldsymbol{\epsilon}_i^*\cdot\boldsymbol{\epsilon}_p\tilde{\psi}^*(t_1 - \delta\tau_{si} - \delta\tau_p, t_2 - \delta\tau_p)\tilde{\phi}(t_3)\end{aligned} \tag{13}$$

where the classical pulse and entangled pulses temporal amplitudes respectively are

$$\tilde{\phi}(t) = \int_{-\infty}^{+\infty} \frac{\mathrm{d}\omega}{2\pi}\phi(\omega)\mathrm{e}^{-i\omega t}$$

and

$$\tilde{\psi}(t_1, t_2) = \int_{-\infty}^{+\infty} \frac{\mathrm{d}\omega_1}{2\pi}\frac{\mathrm{d}\omega_2}{2\pi}\psi(\omega_1, \omega_2)\mathrm{e}^{-i\omega_1 t_1 - i\omega_2 t_2}$$

Hereafter, we assume the following frequency profiles for the classical pump pulse $(\phi(\omega_p))$ and the entangled photon pulses $(\psi(\omega_s, \omega_i))$ as

$$\begin{aligned}\phi(\omega_p) &= \sqrt{I_p}\sqrt{\frac{\sigma_p^2}{2\pi}}\, e^{-\sigma_p^2(\omega_p - \bar{\omega}_p)^2/2} \\ \psi(\omega_s, \omega_i) &= C\phi(\omega_s + \omega_i)\mathrm{sinc}\left(\frac{(\omega_s - \omega_i - \bar{\omega}_s + \bar{\omega}_i)}{4}T_e\right) e^{i[(\omega_s - \omega_i - \bar{\omega}_s + \bar{\omega}_i)/4]T_e}\end{aligned} \tag{14}$$

where the profile of the pulses $\mathbf{P}_1$ and $\mathbf{P}_2$ are identical, with the central frequency $\bar{\omega}_p$, temporal width σ_p, and intensity I_p. Central frequencies of $\mathbf{S}_2$ and $\mathbf{I}$ are respectively $\bar{\omega}_s$ and $\bar{\omega}_i = \bar{\omega}_p - \bar{\omega}_s$. The constant C contains the details of the nonlinear crystal used to generate entangled photons, and T_e is the entanglement time.

Note that the contribution from diagram in Figure 4 $(\mathcal{S}_0^2)$ to $\mathcal{S}_0$ can be suppressed for $\delta\tau_p \gg \sigma_p$, i.e., by reducing the temporal overlap of the pump pulse $\mathbf{P}_1$ and the idler pulse $\mathbf{I}$.

With this, the quantum signals become

https://doi.org/10.1021/acs.jpclett.3c02341
J. Phys. Chem. Lett. 2023, 14, 10803−10809

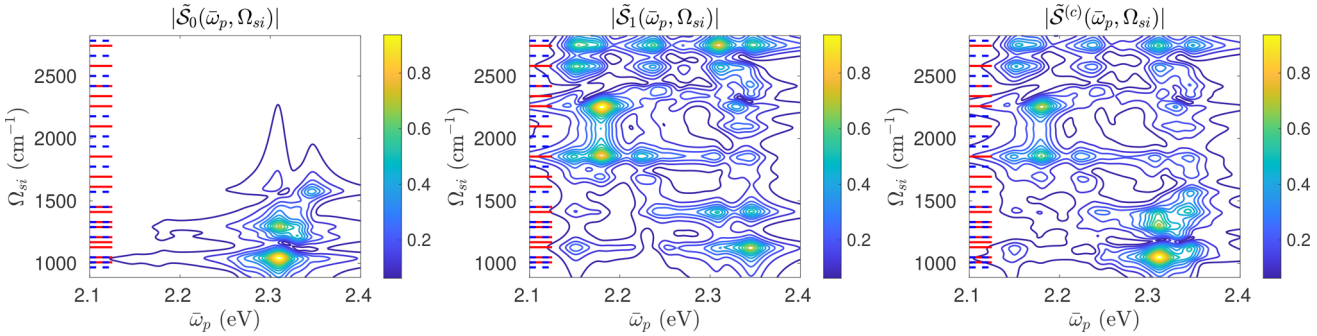

Figure 5. (Normalized) quantum signals, $|\tilde{S}_0|$ (eq 17 and diagram Figure 4 (S_0^1)) and $|\tilde{S}_1|$ (eq 18 and diagram Figure 4 (S_1)) and the classical signal, $|\tilde{S}^{(c)}|$ (their sum), are displayed from left to right. The signals are computed for a two-level vibronic model system with ground and excited states, each having $N = 11$ vibrational states. Red and dashed blue markers indicate allowed vibrational transitions in the ground and excited manifolds, respectively. The interstate vibronic dephasing rate is $\gamma_{e_n g_{n'}} = \gamma_{g_n e_{n'}} = 0.01$ eV and intrastate vibrational dephasing rate is $\gamma_{g_n g_{n'}} = \gamma_{e_n e_{n'}} = 0.005$ eV.

$$S_0(\bar{\omega}_p, \delta\tau_{si}) = -\frac{2\pi C c_{s_2} c_{p_1} c_f \boldsymbol{\epsilon}_s^* \times \boldsymbol{\epsilon}_i^* \cdot \boldsymbol{\epsilon}_p}{3!\hbar^3} \int_{-\infty}^{+\infty} d\omega_s d\omega_p \psi^*(\omega_s, \omega_p - \omega_s)\phi(\omega_p) e^{-i\omega_s \delta\tau_{si} - i\omega_p \delta\tau_p} \int_0^{\infty} d\tau_{12} d\tau_{23} \langle \boldsymbol{V}_L(\tau_{12} + \tau_{23}) \times \boldsymbol{V}_R(\tau_{23}) \cdot \boldsymbol{V}_L^{\dagger}(0) \rangle_s e^{i\omega_s \tau_{12} + i\omega_p \tau_{23}} \tag{15}$$

and

$$S_1(\bar{\omega}_p, \delta\tau_{si}) = \frac{2\pi C c_{s_2} c_{p_1} c_f \boldsymbol{\epsilon}_s^* \times \boldsymbol{\epsilon}_i^* \cdot \boldsymbol{\epsilon}_p}{3!\hbar^3} \int_{-\infty}^{+\infty} d\omega_s d\omega_p \psi^*(\omega_s, \omega_p - \omega_s)\phi(\omega_p) e^{-i\omega_s \delta\tau_{si} - i\omega_p \delta\tau_p} \int_0^{\infty} d\tau_{12} d\tau_{23} \langle \boldsymbol{V}_L(\tau_{12} + \tau_{23}) \times \boldsymbol{V}_L(\tau_{23}) \cdot \boldsymbol{V}_L^{\dagger}(0) \rangle_s e^{i\omega_s \tau_{12} + i\omega_p \tau_{23}} \tag{16}$$

We note that these rotationally averaged signals do not vanish only if the three polarization vectors $\boldsymbol{\epsilon}_p$, $\boldsymbol{\epsilon}_i^*$, and $\boldsymbol{\epsilon}_s^*$ are not coplanar.

The two quantum signals isolate the two main contributions to the classical signal, as represented by the ladder diagrams in Figures 4 (S_0^1) and 4 (S_0^2). Such selectivity is not possible by classical spectroscopy. In the ladder diagrams of Figures 4 (S_0^1) and 4 (S_0^2), it is assumed that the central frequencies of the pulses $\mathbf{P_1}$ ($\bar{\omega}_p$) and $\mathbf{I}$ ($\bar{\omega}_i = \bar{\omega}_p - \bar{\omega}_s$) are in the UV regime, resonant with intermanifold vibronic transitions and that of $\mathbf{S_2}$ ($\bar{\omega}_s$) in the IR regime, resonant with intramanifold vibrational transitions. The time interval τ_{12} in S_0 and S_1 (eqs 15 and 16, respectively), which gives information on excited and ground state vibrational coherence, can be measured with the temporal resolution limited only by the entanglement time (T_e) by scanning $\delta\tau_{si}$. The time interval τ_{23} gives information about the intermanifold vibronic coherence. Close to the CW limit, $\sigma_p \gg 1$, one can select a specific vibronic state, $|e_n\rangle$, by tuning central frequency of the pumps ($\bar{\omega}_p$).

Below the quantum signals, S_0 and S_1 are displayed by a half Fourier transform with respect to $\delta\tau_{si}$,

$$\tilde{S}_{0/1}(\bar{\omega}_p, \Omega_{si}) = \int_0^{\infty} d\delta\tau_{si} e^{i(\Omega_{si} + \bar{\omega}_s)\delta\tau_{si}} S_{0/1}(\bar{\omega}_p, \delta\tau_{si})$$

The sum over states expressions for the quantum signals are given by

$$\tilde{S}_0(\bar{\omega}_p, \Omega_{si}) = \tilde{C} I_p \sum_{n_e, n_e'} \frac{1}{\bar{\omega}_p - (\omega_{e_{n_e}} - \omega_{g_1}) + i\gamma_{e_{n_e} g_1}} \times \frac{\boldsymbol{\mu}_{e_{n_e'} e_{n_e}} \cdot \boldsymbol{\mu}_{g_1 e_{n_e'}} \times \boldsymbol{\mu}_{e_{n_e} g_1}}{\Omega_{si} - (\omega_{e_{n_e}} - \omega_{e_{n_e'}}) + i\gamma_{e_{n_e} e_{n_e'}}} \tag{17}$$

and

$$\tilde{S}_1(\bar{\omega}_p, \Omega_{si}) = -\tilde{C} I_p \sum_{n_e, n_g} \frac{1}{\bar{\omega}_p - (\omega_{e_{n_e}} - \omega_{g_1}) + i\gamma_{e_{n_e} g_1}} \times \frac{\boldsymbol{\mu}_{g_1 g_{n_g}} \cdot \boldsymbol{\mu}_{g_{n_g} e_{n_e}} \times \boldsymbol{\mu}_{e_{n_e} g_1}}{\Omega_{si} - (\omega_{g_{n_g}} - \omega_{g_1}) + i\gamma_{g_{n_g} g_1}} \tag{18}$$

where we have grouped all the inessential factors from eqs 15 and 16 into $\tilde{C}$. Moreover, we have introduced phenomenological dephasing rates $\gamma_{\sigma_n \sigma_{n'}}$. We also assumed $\gamma_{\sigma_n \sigma_{n'}} T_e \ll 1$ and $\sigma_p^{-1} \approx 0$.

The sum over states expression for the classical signal derived in Supporting Information is

$$\tilde{S}^{(c)}(\bar{\omega}_p, \Omega_{si}) = \bar{C} I_p^{3/2} \sum_{n_e} \frac{1}{\bar{\omega}_p - (\omega_{e_{n_e}} - \omega_{g_1}) + i\gamma_{e_{n_e} g_1}} \times \left(\sum_{n_e'} \frac{\boldsymbol{\mu}_{e_{n_e'} e_{n_e}} \cdot \boldsymbol{\mu}_{g_1 e_{n_e'}} \times \boldsymbol{\mu}_{e_{n_e} g_1}}{\Omega_{si} - (\omega_{e_{n_e}} - \omega_{e_{n_e'}}) + i\gamma_{e_{n_e} e_{n_e'}}} - \sum_{n_g} \frac{\boldsymbol{\mu}_{g_1 g_{n_g}} \cdot \boldsymbol{\mu}_{g_{n_g} e_{n_e}} \times \boldsymbol{\mu}_{e_{n_e} g_1}}{\Omega_{si} - (\omega_{g_{n_g}} - \omega_{g_1}) + i\gamma_{g_{n_g} g_1}} \right) \tag{19}$$

Note that the classical signal (eq 19) scales with the input intensity as $I_p^{3/2}$, whereas the quantum signals (eqs 17 and 18) scale as I_p and therefore are enhanced at low intensities.

We now compare the quantum signals and the classical DFG signals for the model system shown in Figure 2. It consists of two energy level manifolds, the ground and excited states, each with $N = 11$ vibrational states. The model system parameters are chosen as follows. The energy gap between the lowest vibrational state in the ground electronic manifold and the lowest vibrational state in the excited electronic manifold is 2 eV. Intramanifold vibrational transitions are in the range 0.14−0.35 eV (see red and blue markers of Figure 5). Components of intermanifold vibronic transition dipole moment vectors are chosen randomly from the normal distribution with zero mean and 1 D standard deviation. Intramanifold transitions between

https://doi.org/10.1021/acs.jpclett.3c02341
J. Phys. Chem. Lett. 2023, 14, 10803−10809

vibrational states with energy gaps less than 0.12 eV are neglected, and the remaining transition dipole moment vector components are chosen randomly from the normal distribution with zero mean and 1 D standard deviation.

The quantum signals $\mathcal{S}_0$ and $\mathcal{S}_1$ and the classical signal $\mathcal{S}^{(c)}$ (eqs 17, 18, and 19, respectively) are displayed in Figure 5. In both the classical signal in eq 19 and the quantum signals in eqs 17 and 18, $\bar{\omega}_p$ scans the inter manifold vibronic transitions ($\omega_{e_n} - \omega_{g_1}$). The classical signal in eq 19 shows resonances at $\omega_{e_n} - \omega_{e_{n'}}$ and $\omega_{g_n} - \omega_{g_1}$ when Ω_{si} is scanned, but these resonances are separated in the quantum signals. $\tilde{\mathcal{S}}_0$ isolates the resonances $\omega_{e_n} - \omega_{e_{n'}}$, whereas $\tilde{\mathcal{S}}_1$ isolates the resonances $\omega_{g_n} - \omega_{g_1}$. This is because in the ladder diagrams, Figure 4 ($\mathcal{S}_0^1$), with evolution of excited state vibrational coherences during second time delay, and Figure 4 ($\mathcal{S}_1$), with evolution of ground state vibrational coherences during second time delay, are selected by $\mathcal{S}_0$ and $\mathcal{S}_1$, respectively. But, both these diagrams contribute to the classical signal $\mathcal{S}^{(c)}$. This is clear from Figure 5, where resonances features in $\tilde{\mathcal{S}}^{(c)}$ are separately monitored by $\tilde{\mathcal{S}}_0$ and $\tilde{\mathcal{S}}_1$. From Figure 5, we see that only low-frequency ($\Omega_{si} < 1800$ cm^{-1}) excited state vibrational transitions appear in $\tilde{\mathcal{S}}_0$, whereas $\tilde{\mathcal{S}}_1$ also contains high frequency vibrational transitions. Moreover, various vibronic−vibrational resonances occurring in the region $\bar{\omega}_p \approx$ 2.25−2.4 eV and $\Omega_{si} \approx$ 1000−1800 cm^{-1} in $\tilde{\mathcal{S}}^{(c)}$ are individually selected by $\tilde{\mathcal{S}}_0$ and $\tilde{\mathcal{S}}_1$ and hence can be interpreted as arising from the vibrational transitions in the excited electronic state and the ground electronic state, respectively. Additional 1D plots demonstrating the advantage of the quantum signals are provided in Figure S2 of the Supporting Information.

The interferometric setup proposed here can be used for selectively probing all of the Liouville space pathways that contribute to ultrafast DFG signals. It can selectively probe the pathways involving vibrational coherences in the excited and ground state manifolds. The time-frequency entanglement can target a specific excited vibronic state while time resolving the dynamics of the vibrational coherences. Due to the linear scaling of quantum signals with pump intensity (as opposed to the higher order scaling of the classical signal), the quantum signals are enhanced for low intensities. The Liouville space pathway selectivity offered by this technique is demonstrated for a model system and by comparing the quantum signals to the classical signal. We note that we have assumed a single photon pulse; however, the proposed experiment can be done with a laser pulse prepared in a low intensity coherent state.

■ ASSOCIATED CONTENT

Supporting Information

The Supporting Information is available free of charge at https://pubs.acs.org/doi/10.1021/acs.jpclett.3c02341.

Detailed description of the light state preparation, the coincidence measurement and the classical DFG signal, and additional 1D plots of the quantum and classical signals (PDF, ZIP)

■ AUTHOR INFORMATION

Corresponding Authors

Shaul Mukamel − *Department of Chemistry, University of California, Irvine, California 92614, United States; Department of Physics and Astronomy, University of California, Irvine, California 92614, United States;* orcid.org/0000-0002-6015-3135; Email: smukamel@uci.edu

Hari Kumar Yadalam − *Department of Chemistry, University of California, Irvine, California 92614, United States; Department of Physics and Astronomy, University of California, Irvine, California 92614, United States;* orcid.org/0000-0001-9340-7683; Email: hyadalam@uci.edu

Authors

Matthias Kizmann − *Department of Chemistry, University of California, Irvine, California 92614, United States; Department of Physics and Astronomy, University of California, Irvine, California 92614, United States*

Jérémy R. Rouxel − *Chemical Sciences and Engineering Division, Argonne National Laboratory, Lemont, Illinois 60439, United States;* orcid.org/0000-0003-3438-6370

Yeonsig Nam − *Department of Chemistry, University of California, Irvine, California 92614, United States; Department of Physics and Astronomy, University of California, Irvine, California 92614, United States;* orcid.org/0000-0003-0386-9118

Vladimir Y. Chernyak − *Department of Chemistry, Wayne State University, Detroit, Michigan 48202, United States; Department of Mathematics, Wayne State University, Detroit, Michigan 48202, United States*

Complete contact information is available at: https://pubs.acs.org/10.1021/acs.jpclett.3c02341

Notes

The authors declare no competing financial interest.

■ ACKNOWLEDGMENTS

VYC and SM gratefully acknowledge the support of the US Department of Energy, Office of Science, Basic Energy Sciences Award DESC0022134, which has primarily funded this work. SM gratefully acknowledges the support of the National Science Foundation (Grant CHE-2246379). MK acknowledges the support from the Alexander von Humboldt Foundation through the Feodor Lynen program. SM is a senior fellow at the Hagler institute of advanced study at Texas A&M. J.R.R. acknowledges support from the U.S. Department of Energy, Office of Science, Basic Energy Science, Chemical Sciences, Geosciences and Biosciences Division under Contract No. DE-AC02-06CH11357.

■ REFERENCES

(1) Bloembergen, N.; Pershan, P. S. Light Waves at the Boundary of Nonlinear Media. *Phys. Rev.* **1962**, *128*, 606−622.

(2) Bloembergen, N. *Nonlinear Optics*, 4th ed.; World Scientific: 1996.

(3) Dick, B.; Hochstrasser, R. M. Spectroscopy Using Sum- and Difference-Frequency Generation in Molecular Solids. *Phys. Rev. Lett.* **1983**, *51*, 2221−2223.

(4) Zhu, X. D.; Suhr, H.; Shen, Y. R. Surface vibrational spectroscopy by infrared-visible sum frequency generation. *Phys. Rev. B* **1987**, *35*, 3047−3050.

(5) Ayuso, D.; Ordonez, A. F.; Smirnova, O. Ultrafast chirality: the road to efficient chiral measurements. *Phys. Chem. Chem. Phys.* **2022**, *24*, 26962−26991.

(6) Giordmaine, J. A. Nonlinear Optical Properties of Liquids. *Phys. Rev.* **1965**, *138*, A1599−A1606.

(7) Heinz, T. F.; Himpsel, F. J.; Palange, E.; Burstein, E. Electronic transitions at the CaF_2/Si(111) interface probed by resonant three-wave mixing spectroscopy. *Phys. Rev. Lett.* **1989**, *63*, 644−647.
(8) Fischer, P.; Wiersma, D. S.; Righini, R.; Champagne, B.; Buckingham, A. D. Three-Wave Mixing in Chiral Liquids. *Phys. Rev. Lett.* **2000**, *85*, 4253−4256.
(9) Choi, J.-H.; Cheon, S.; Lee, H.; Cho, M. Two-dimensional nonlinear optical activity spectroscopy of coupled multi-chromophore system. *Phys. Chem. Chem. Phys.* **2008**, *10*, 3839−3856.
(10) Mukamel, S. *Principles of nonlinear optical spectroscopy*; Oxford University Press: 1995.
(11) Cho, M. *Two-dimensional optical spectroscopy*; CRC Press: 2009.
(12) Dick, B.; Hochstrasser, R. M. Spectroscopic and line-narrowing properties of resonant sum and difference frequency generation. *J. Chem. Phys.* **1983**, *78*, 3398−3409.
(13) Venkatramani, R.; Mukamel, S. Correlated line broadening in multidimensional vibrational spectroscopy. *J. Chem. Phys.* **2002**, *117*, 11089−11101.
(14) Dorfman, K. E.; Schlawin, F.; Mukamel, S. Nonlinear optical signals and spectroscopy with quantum light. *Rev. Mod. Phys.* **2016**, *88*, 045008.
(15) Mukamel, S.; Freyberger, M.; Schleich, W.; Bellini, M.; Zavatta, A.; Leuchs, G.; Silberhorn, C.; Boyd, R. W.; Sánchez-Soto, L. L.; Stefanov, A.; et al. Roadmap on quantum light spectroscopy. *Journal of physics B: Atomic, molecular and optical physics* **2020**, *53*, 072002.
(16) Szoke, S.; Liu, H.; Hickam, B. P.; He, M.; Cushing, S. K. Entangled light−matter interactions and spectroscopy. *Journal of Materials Chemistry C* **2020**, *8*, 10732−10741.
(17) Eshun, A.; Varnavski, O.; Villabona-Monsalve, J. P.; Burdick, R. K.; Goodson, T., III Entangled photon spectroscopy. *Acc. Chem. Res.* **2022**, *55*, 991−1003.
(18) Raymer, M. G.; Landes, T.; Marcus, A. H. Entangled two-photon absorption by atoms and molecules: A quantum optics tutorial. *J. Chem. Phys.* **2021**, *155*, 081501.
(19) Schlawin, F.; Dorfman, K. E.; Mukamel, S. Entangled two-photon absorption spectroscopy. *Accounts of chemical research* **2018**, *51*, 2207−2214.
(20) Gea-Banacloche, J. Two-photon absorption of nonclassical light. *Phys. Rev. Lett.* **1989**, *62*, 1603−1606.
(21) Javanainen, J.; Gould, P. L. Linear intensity dependence of a two-photon transition rate. *Phys. Rev. A* **1990**, *41*, 5088−5091.
(22) Georgiades, N. P.; Polzik, E. S.; Edamatsu, K.; Kimble, H. J.; Parkins, A. S. Nonclassical Excitation for Atoms in a Squeezed Vacuum. *Phys. Rev. Lett.* **1995**, *75*, 3426−3429.
(23) Georgiades, N. P.; Polzik, E. S.; Kimble, H. J. Atoms as nonlinear mixers for detection of quantum correlations at ultrahigh frequencies. *Phys. Rev. A* **1997**, *55*, R1605−R1608.
(24) Dayan, B.; Pe'er, A.; Friesem, A. A.; Silberberg, Y. Two Photon Absorption and Coherent Control with Broadband Down-Converted Light. *Phys. Rev. Lett.* **2004**, *93*, 023005.
(25) Lee, D.-I.; Goodson, T. Entangled photon absorption in an organic porphyrin dendrimer. *J. Phys. Chem. B* **2006**, *110*, 25582−25585.
(26) Roslyak, O.; Mukamel, S. Multidimensional pump-probe spectroscopy with entangled twin-photon states. *Phys. Rev. A* **2009**, *79*, 063409.
(27) Richter, M.; Mukamel, S. Ultrafast double-quantum-coherence spectroscopy of excitons with entangled photons. *Phys. Rev. A* **2010**, *82*, 013820.
(28) Svidzinsky, A.; Agarwal, G.; Classen, A.; Sokolov, A. V.; Zheltikov, A.; Zubairy, M. S.; Scully, M. O. Enhancing stimulated Raman excitation and two-photon absorption using entangled states of light. *Phys. Rev. Res.* **2021**, *3*, 043029.
(29) Pan, J.-W.; Chen, Z.-B.; Lu, C.-Y.; Weinfurter, H.; Zeilinger, A.; Żukowski, M. Multiphoton entanglement and interferometry. *Rev. Mod. Phys.* **2012**, *84*, 777−838.
(30) Ou, Z. Y.; Li, X. Quantum SU(1,1) interferometers: Basic principles and applications. *APL Photonics* **2020**, *5*, 080902.
(31) Chekhova, M. V.; Ou, Z. Y. Nonlinear interferometers in quantum optics. *Adv. Opt. Photon.* **2016**, *8*, 104−155.
(32) Raymer, M. G.; Marcus, A. H.; Widom, J. R.; Vitullo, D. L. Entangled photon-pair two-dimensional fluorescence spectroscopy (EPP-2DFS). *J. Phys. Chem. B* **2013**, *117*, 15559−15575.
(33) Schlawin, F.; Dorfman, K. E.; Mukamel, S. Pump-probe spectroscopy using quantum light with two-photon coincidence detection. *Phys. Rev. A* **2016**, *93*, 023807.
(34) Dorfman, K. E.; Asban, S.; Gu, B.; Mukamel, S. Hong-Ou-Mandel interferometry and spectroscopy using entangled photons. *Communications Physics* **2021**, *4*, 49.
(35) Asban, S.; Mukamel, S. Distinguishability and "which pathway" information in multidimensional interferometric spectroscopy with a single entangled photon-pair. *Science Advances* **2021**, *7*, No. eabj4566.
(36) Asban, S.; Chernyak, V. Y.; Mukamel, S. Nonlinear quantum interferometric spectroscopy with entangled photon pairs. *J. Chem. Phys.* **2022**, *156*, 094202.
(37) Liu, X.; Li, T.; Wang, J.; Kamble, M. R.; Zheltikov, A. M.; Agarwal, G. S. Probing ultra-fast dephasing via entangled photon pairs. *Opt. Express* **2022**, *30*, 47463−47474.
(38) Kizmann, M.; Yadalam, H. K.; Chernyak, V. Y.; Mukamel, S. Quantum interferometry and pathway selectivity in the nonlinear response of photosynthetic excitons. *Proc. Natl. Acad. Sci. U. S. A.* **2023**, *120*, No. e2304737120.
(39) Dorfman, K. E.; Schlawin, F.; Mukamel, S. Stimulated Raman spectroscopy with entangled light: enhanced resolution and pathway selection. *journal of physical chemistry letters* **2014**, *5*, 2843−2849.
(40) Zou, X. Y.; Wang, L. J.; Mandel, L. Induced coherence and indistinguishability in optical interference. *Phys. Rev. Lett.* **1991**, *67*, 318−321.
(41) Wang, L. J.; Zou, X. Y.; Mandel, L. Induced coherence without induced emission. *Phys. Rev. A* **1991**, *44*, 4614−4622.
(42) Hochrainer, A.; Lahiri, M.; Erhard, M.; Krenn, M.; Zeilinger, A. Quantum indistinguishability by path identity and with undetected photons. *Rev. Mod. Phys.* **2022**, *94*, 025007.
(43) Lemos, G. B.; Borish, V.; Cole, G. D.; Ramelow, S.; Lapkiewicz, R.; Zeilinger, A. Quantum imaging with undetected photons. *Nature* **2014**, *512*, 409−412.
(44) Kalashnikov, D. A.; Paterova, A. V.; Kulik, S. P.; Krivitsky, L. A. Infrared spectroscopy with visible light. *Nat. Photonics* **2016**, *10*, 98−101.
(45) Lee, S. K.; Yoon, T. H.; Cho, M. Interferometric quantum spectroscopy with undetected photons via distinguishability modulation. *Opt. Express* **2019**, *27*, 14853−14870.
(46) Roslyak, O.; Mukamel, S. A unified description of sum frequency generation, parametric down conversion and two-photon fluorescence. *Molecular physics* **2009**, *107*, 265−280.
(47) Mukamel, S. Superoperator representation of nonlinear response: Unifying quantum field and mode coupling theories. *Phys. Rev. E* **2003**, *68*, 021111.
(48) Mukamel, S. Partially-time-ordered Schwinger-Keldysh loop expansion of coherent nonlinear optical susceptibilities. *Phys. Rev. A* **2008**, *77*, 023801.
(49) Andrews, D. L.; Thirunamachandran, T. On three-dimensional rotational averages. *J. Chem. Phys.* **1977**, *67*, 5026−5033.

https://doi.org/10.1021/acs.jpclett.3c02341
J. Phys. Chem. Lett. 2023, 14, 10803−10809

Supplementary: Quantum Interferometric Pathway Selectivity in Difference-Frequency-Generation Spectroscopy

Hari Kumar Yadalam,[*,†,‡] Matthias Kizmann,[*,†,‡] Jérémy R. Rouxel,[*,¶] Yeonsig Nam,[*,†,‡] Vladimir Y. Chernyak,[*,§,‖] and Shaul Mukamel[*,†,‡]

†*Department of Chemistry, University of California, Irvine, CA 92614, USA*
‡*Department of Physics and Astronomy, University of California, Irvine, CA 92614, USA*
¶*Chemical Sciences and Engineering Division, Argonne National Laboratory, Lemont, Illinois 60439, USA*
§*Department of Chemistry, Wayne State University, 5101 Cass Ave, Detroit, Michigan 48202, USA*
‖*Department of Mathematics, Wayne State University, 656 W. Kirby, Detroit, Michigan 48202, USA*

The light state preparation

Weak coherent light pulse along the optical path $\mathbf{P}$ with polarization $\boldsymbol{\epsilon}_p$ is described by the state,

$$|\Psi(-\infty)\rangle = e^{\int_{-\infty}^{+\infty} d\omega_p \, \left[\phi(\omega_p) a^\dagger_{p\boldsymbol{\epsilon}_p}(\omega_p) - \phi^*(\omega_p) a_{p\boldsymbol{\epsilon}_p}(\omega_p)\right]} |\varnothing\rangle$$

$$|\Psi(-\infty)\rangle \approx \int_{-\infty}^{+\infty} d\omega_p \; \phi(\omega_p) a^\dagger_{p\boldsymbol{\epsilon}_p}(\omega_p)|\varnothing\rangle, \quad (1)$$

where $|\varnothing\rangle$ is the vacuum state of the electromagnetic field. $a_{p\boldsymbol{\epsilon}_p}(\omega_p)$ is an annihilation operator representing monochromatic electromagnetic field mode with frequency ω_p propagating along the optical path $\mathbf{P}$ and with the polarization $\boldsymbol{\epsilon}_p$. In the second line, we assumed that the light intensity is very weak ($|\phi(\omega_p)|^2 \ll 1$), and hence, upon conditioning that at least a photon is present in the pulse, can be approximated with an unnormalized single photon state.

A beam splitter then splits $\mathbf{P}$ into two pulses along the optical paths $\mathbf{P_1}$ and $\mathbf{P_2}$ with same polarization. A variable time delay $\delta\tau_p$ is introduced between these two pulses. The state of light in these two pulses is then,

$$|\Psi(-\infty)\rangle = \frac{1}{\sqrt{2}} \int_{-\infty}^{+\infty} d\omega_p \, \phi(\omega_p) \left[a^\dagger_{p_1\boldsymbol{\epsilon}_p}(\omega_p) - i a^\dagger_{p_2\boldsymbol{\epsilon}_p}(\omega_p) e^{i\omega_p \delta\tau_p}\right] |\varnothing\rangle. \quad (2)$$

The light pulse $\mathbf{P_2}$ then goes through a parametric downconverter, **PDC**, to generate an entangled photon pulse pair along the optical paths $\mathbf{I}$ and $\mathbf{S_2}$ with their respective polarizations $\boldsymbol{\epsilon}_i$ and $\boldsymbol{\epsilon}_s$. A time delay $\delta\tau_{si}$ is introduced between these two pulses.

The final state of light in the pulses $\mathbf{P_1}$, $\mathbf{I}$ and

$\mathbf{S_2}$ is then given by,

$$|\Psi(-\infty)\rangle = \frac{1}{\sqrt{2}}\Big[\int_{-\infty}^{+\infty} d\omega_p\ \phi(\omega_p) a^\dagger_{p_1\boldsymbol{\epsilon}_p}(\omega_p) + \int_{-\infty}^{+\infty} d\omega_s d\omega_i\ \psi(\omega_s,\omega_i) e^{i\omega_i\delta\tau_p + i\omega_s(\delta\tau_p+\delta\tau_{si})} a^\dagger_{s_2\boldsymbol{\epsilon}_s}(\omega_s) a^\dagger_{i\boldsymbol{\epsilon}_i}(\omega_i)\Big]|\varnothing\rangle. \quad (3)$$

The coincidence measurement

The proposed coincidence measurement detects in coincidence: (i) Photon number resolved detection of the pulse $\mathbf{I}$ at the detector $\mathbf{D_I}$, and (ii) Difference of counts of a single photon detected at the detectors $\mathbf{D_{S_1}}$ and $\mathbf{D_{S_2}}$, which measures single photon coherence (heterodyne) between photons in pulses $\tilde{\mathbf{S}}_\mathbf{1}$ and $\tilde{\mathbf{S}}_\mathbf{2}$. This coincidence detection of n_i photons in idler along with heterodyne of $\tilde{\mathbf{S}}_\mathbf{1}$ and $\tilde{\mathbf{S}}_\mathbf{2}$ gives the signal,

$$\mathcal{S}_{n_i} = \int_{-\infty}^{+\infty} dt_s \langle \mathcal{T} \sum_{\lambda_s} \Big(\bar{a}^\dagger_{\tilde{s}_1\boldsymbol{\epsilon}_{\lambda_s}R}(t_s)\bar{a}_{\tilde{s}_1\boldsymbol{\epsilon}_{\lambda_s}L}(t_s) - \bar{a}^\dagger_{\tilde{s}_2\boldsymbol{\epsilon}_{\lambda_s}R}(t_s)\bar{a}_{\tilde{s}_2\boldsymbol{\epsilon}_{\lambda_s}L}(t_s)\Big) \times \Bigg\{\frac{1}{n_i!}\left(\int_{-\infty}^{+\infty} dt_i \sum_{\lambda_i} \bar{a}^\dagger_{i\boldsymbol{\epsilon}_{\lambda_i}R}(t_i)\bar{a}_{i\boldsymbol{\epsilon}_{\lambda_i}L}(t_i)\right)^{n_i} e^{-\int_{-\infty}^{+\infty} dt_i \sum_{\lambda_i} \bar{a}^\dagger_{i\boldsymbol{\epsilon}_{\lambda_i}R}(t_i)\bar{a}_{i\boldsymbol{\epsilon}_{\lambda_i}L}(t_i)}\Bigg\}\rangle. \quad (4)$$

Here $\bar{a}_{\alpha\boldsymbol{\epsilon}}(t)$ is the interaction-picture operator given by $\bar{a}_{\alpha\boldsymbol{\epsilon}}(t) = \frac{1}{\sqrt{2\pi}}\int_{-\infty}^{+\infty} d\omega a_{\alpha\boldsymbol{\epsilon}}(\omega)e^{-i\omega t}$. Furthermore, $\langle \mathcal{T}\cdots\rangle$ corresponds to average with respect to the joint density matrix of the sample and electromagnetic field in the interaction picture.

Expressing the operators for photons in pulses $\tilde{\mathbf{S}}_{\mathbf{1/2}}$ at the detectors $\mathbf{D}_{\mathbf{S_{1/2}}}$ in terms of the operators for photons in the pulses $\mathbf{S_{1/2}}$ using the $50-50$ beam splitter transformation, $\begin{pmatrix}\bar{a}_{\tilde{s}_1\boldsymbol{\epsilon}}(t)\\ \bar{a}_{\tilde{s}_2\boldsymbol{\epsilon}}(t)\end{pmatrix} = \frac{1}{\sqrt{2}}\begin{pmatrix}1 & i\\ i & 1\end{pmatrix}\begin{pmatrix}\bar{a}_{s_1\boldsymbol{\epsilon}}(t)\\ \bar{a}_{s_2\boldsymbol{\epsilon}}(t)\end{pmatrix}$, gives the signal as,

$$\mathcal{S}_{n_i} = 2\mathrm{Im}\int_{-\infty}^{+\infty} dt_s \langle \mathcal{T} \sum_{\lambda_s} \bar{a}^\dagger_{s_2\boldsymbol{\epsilon}_{\lambda_s}R}(t_s)\bar{a}_{s_1\boldsymbol{\epsilon}_{\lambda_s}L}(t_s) \Bigg\{\frac{1}{n_i!}\left(\int_{-\infty}^{+\infty} dt_i \sum_{\lambda_i} \bar{a}^\dagger_{i\boldsymbol{\epsilon}_{\lambda_i}R}(t_i)\bar{a}_{i\boldsymbol{\epsilon}_{\lambda_i}L}(t_i)\right)^{n_i} e^{-\int_{-\infty}^{+\infty} dt_i \sum_{\lambda_i} \bar{a}^\dagger_{i\boldsymbol{\epsilon}_{\lambda_i}R}(t_i)\bar{a}_{i\boldsymbol{\epsilon}_{\lambda_i}L}(t_i)}\Bigg\}\rangle. \quad (5)$$

The motivation for this coincidence signal is as follows. The low intensity coherent pulse $\mathbf{P}$, approximated as a single photon pulse, is split in to two pulses, $\mathbf{P_1}$ and $\mathbf{P_2}$, such that a photon is either in one or the other pulse but not both. $\mathbf{P_1}$ interacts with the sample and $\mathbf{P_2}$ interacts with the PDC crystal, shown in Fig. (1) of the main text. Noting that the above coincidence detects the coherence between a photon in the pulses $\mathbf{S_1}$ and $\mathbf{S_2}$ in coincidence with photon number resolved detection of idler photons, two possible processes represented by the Feynman diagrams in Fig. (S1) can happen at the sample and the crystal. Both processes involve coherences between the single photon pulses $\mathbf{P_1}$ and $\mathbf{P_2}$. The two processes are:

(i) By the process described by Feynman and loop diagrams in Fig. (S1.$\mathcal{S}_0$), a photon from $\mathbf{P_1}$ is annihilated and the molecular ket is excited and a photon in pulse $\mathbf{P_2}$ is down converted at the crystal by generating time ordered idler and signal photon pulses $\mathbf{I}$ and $\mathbf{S_2}$ respectively on the right (bra) side of the density matrix. The idler photon generated in pulse $\mathbf{I}$ at the crystal on the right side is annihilated at the sample by creating an excitation on the right side in the sample. Upon de-excitation on the left side in the sample, a photon is generated in the pulse $\mathbf{S_1}$ on the left side. This coherence between a photon in the pulse $\mathbf{S_1}$ on the left side and the pulse $\mathbf{S_2}$ on the right side, created in coherence at sample and crystal, is detected by the detectors $\mathbf{D_{S_1}}$ and $\mathbf{D_{S_2}}$ and zero photons are detected in the pulse $\mathbf{I}$ at the detector $\mathbf{D_I}$. The two possible photon counts recorded

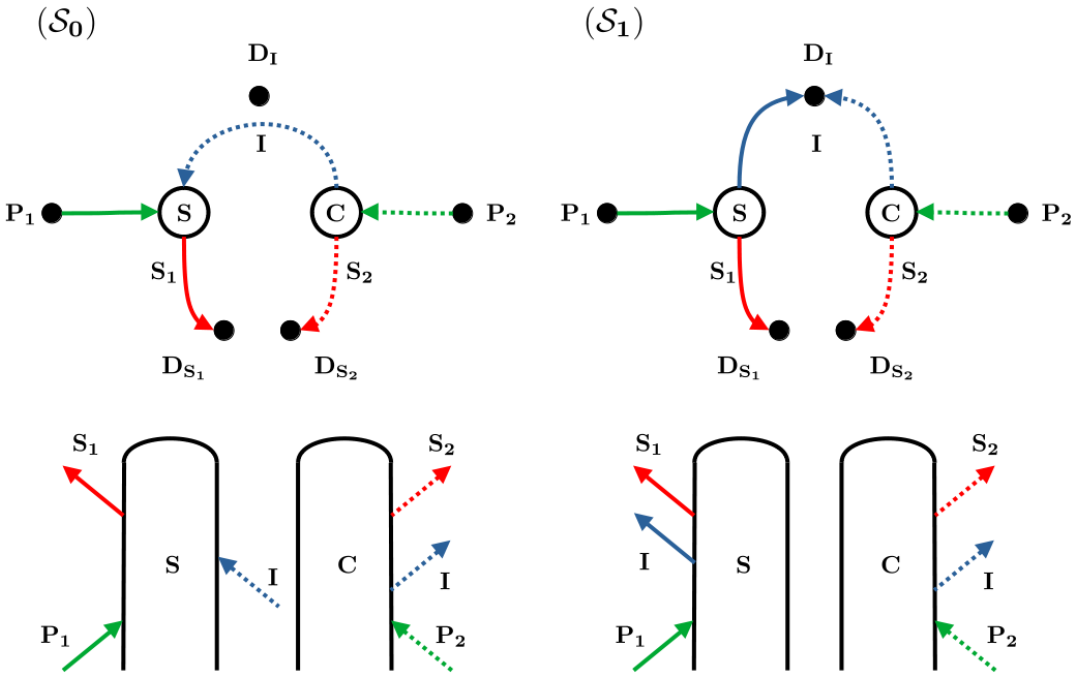

Figure S1: Feynman diagrams on Keldysh loop and the corresponding loop diagrams for sample and crystal. Diagrams $(\mathcal{S}_0)$ and $(\mathcal{S}_1)$ contribute to the signals $\mathcal{S}_0$ and $\mathcal{S}_1$ respectively.

at the three detectors corresponding to this process are summarized in the first two rows of the Tab. (I) of the main text.

(ii) By the process described by Feynman and loop diagrams in Fig. (S1.$\mathcal{S}_1$), the coherence between photons in pulses $\mathbf{P_1}$ and $\mathbf{P_2}$, with a photon in pulse $\mathbf{P_1}$ on the left side and the pulse $\mathbf{P_2}$ on the right side, respectively interact with sample and crystal. A series of resonant transitions at the sample on the ket side and off resonant processes at the crystal on the bra side, generate a photon in pulse $\mathbf{I}$ on both left and right sides and a coherence between photons in the pulses $\mathbf{S_1}$ and $\mathbf{S_2}$. This coherence between photon in pulses $\mathbf{S_1}$ and $\mathbf{S_2}$ is detected by the detectors $\mathbf{D_{S_1}}$ and $\mathbf{D_{S_2}}$ and a photon in the pulse $\mathbf{I}$ is detected at the detector $\mathbf{D_I}$. The two possible photon counts recorded at the three detectors corresponding to this second process are summarized in the last two rows of the Tab. (I) of the main text.

We note that in the above, we only considered the loop diagram for the crystal with all interactions on one side, because, the other loop diagram with two interactions on one side and one on the other side is typically off resonant. Moreover, as there are no photons in idler or signal pulses in the initial field state, such a process does not contribute.

As it is clear from above, because the pulse $\mathbf{I}$ has at the most one photon, $\mathcal{S}_{n_i}$ is non vanishing only for $n_i = 0, 1$.

Expressing the above coincidence signal in terms of electric field vector operators defined below Eq. (5) of the main text, gives,

$$\mathcal{S}_{n_i} = 2\mathrm{Im}\frac{1}{2\pi c_{s1}c_{s2}}\int_{-\infty}^{+\infty} dt_s \langle \mathcal{T}\boldsymbol{\mathcal{E}}^{\dagger}_{s_2R}(t_s)\cdot\boldsymbol{\mathcal{E}}_{s_1L}(t_s) \left\{\frac{1}{n_i!}\left(\frac{1}{2\pi c_i^2}\int_{-\infty}^{+\infty} dt_i \boldsymbol{\mathcal{E}}^{\dagger}_{iR}(t_i)\cdot\boldsymbol{\mathcal{E}}_{iL}(t_i)\right)^{n_i} e^{-\frac{1}{2\pi c_i^2}\int_{-\infty}^{+\infty} dt_i \boldsymbol{\mathcal{E}}^{\dagger}_{iR}(t_i)\cdot\boldsymbol{\mathcal{E}}_{iL}(t_i)}\right\}\rangle. \quad (6)$$

Expanding this equation up to linear order in the number operator of the idler pulse leads to Eqs. (6) and (7) of the main text.

The classical ultrafast DFG signal

The classical time resolved difference frequency generation technique with heterodyne detection uses three time ordered pulses, in the order $\tilde{\boldsymbol{E}}_p(t)$, $\tilde{\boldsymbol{E}}_i(t)$ and $\tilde{\boldsymbol{E}}_s(t)$, with well separated temporal profiles. The total electric field amplitude is given by,

$$\tilde{\boldsymbol{E}}(t) = \tilde{\boldsymbol{E}}_s(t-\delta\tau_{si}-\delta\tau_p)+\tilde{\boldsymbol{E}}_i(t-\delta\tau_p)+\tilde{\boldsymbol{E}}_p(t). \tag{7}$$

We note that we have chosen to keep labels for the pulses to be consistent with quantum case. $\delta\tau_p$ is time delay between pulses i and p and $\delta\tau_{si}$ is between s and i.

The rotationally averaged classical heterodyne difference frequency generation signal is given by,

$$\mathcal{S}^{(c)} = \frac{2}{3!}\mathrm{Im}\left(-\frac{i}{\hbar}\right)^3 \int_{-\infty}^{+\infty} dt_1 dt_2 dt_3$$
$$\tilde{\boldsymbol{E}}_s^*(t_1)\times\tilde{\boldsymbol{E}}_i^*(t_2)\cdot\tilde{\boldsymbol{E}}_p(t_3)\big[\langle\mathcal{T}\boldsymbol{V}_L(t_1)\times\boldsymbol{V}_L(t_2)\cdot\boldsymbol{V}_L^\dagger(t_3)\rangle_s$$
$$-\langle\mathcal{T}\boldsymbol{V}_L(t_1)\times\boldsymbol{V}_R(t_2)\cdot\boldsymbol{V}_L^\dagger(t_3)\rangle_s\big]. \tag{8}$$

Clearly, the above classical signal has contributions from both the loop diagrams shown in Fig. (3) of the main text, and hence has contributions from all the three ladder diagrams shown in Fig. (4) of the main text.

We assume the following gaussian frequency domain profiles for the pulses,

$$\boldsymbol{E}_\alpha(\omega) = \int_{-\infty}^{+\infty} dt e^{i\omega t}\tilde{\boldsymbol{E}}_\alpha(t) = i\sqrt{I_\alpha}\sqrt{\frac{\sigma_\alpha^2}{2\pi}}e^{-\sigma_\alpha^2\frac{(\omega-\bar{\omega}_\alpha)^2}{2}}. \tag{9}$$

Here σ_α, $\bar{\omega}_\alpha$ and I_α are respectively temporal width, central frequency and intensity of the α pulse. Moreover, the central frequencies are chosen to satisfy $\bar{\omega}_i = \bar{\omega}_p - \bar{\omega}_s$.

Similar to the quantum signals, we can suppress the contribution from the ladder diagram shown in Fig. (4.$\mathcal{S}_0^2$) of the main text by choosing $\delta\tau_p \gg \sigma_p$.

With this, the above signal can be written as,

$$\mathcal{S}^{(c)}(\bar{\omega}_p, \delta\tau_{si}) = \frac{1}{12\pi^2}\mathrm{Im}\left(-\frac{i}{\hbar}\right)^3$$
$$\int_{-\infty}^{+\infty} d\omega_s d\omega_p \boldsymbol{E}_s^*(\omega_s)\times\boldsymbol{E}_i^*(\omega_p-\omega_s)\cdot\boldsymbol{E}_p(\omega_p)e^{-i\omega_s\delta\tau_{si}-i\omega_p\delta\tau_p}$$
$$\int_0^\infty d\tau_{12}d\tau_{23}\big[\langle\boldsymbol{V}_L(\tau_{12}+\tau_{23})\times\boldsymbol{V}_L(\tau_{23})\cdot\boldsymbol{V}_L^\dagger(0)\rangle_s$$
$$-\langle\boldsymbol{V}_L(\tau_{12}+\tau_{23})\times\boldsymbol{V}_R(\tau_{23})\cdot\boldsymbol{V}_L^\dagger(0)\rangle_s\big]e^{i\omega_s\tau_{12}+i\omega_p\tau_{23}}. \tag{10}$$

Note that here we have only shown explicit dependence of the signal on $\bar{\omega}_p$ and $\delta\tau_{si}$, as we scan these parameters while keeping others fixed to obtain spectral information of the system.

The signal is conveniently studied by half fourier transforming it with respect to $\delta\tau_{12}$ as,

$$\tilde{\mathcal{S}}^{(c)}(\bar{\omega}_p, \Omega_{si}) = \int_0^\infty d\delta\tau_{12}\, e^{i(\Omega_{si}+\bar{\omega}_s)\delta\tau_{12}}\mathcal{S}^{(c)}(\bar{\omega}_p, \delta\tau_{si}).$$

We further assume that $\sigma_p^{-1} \approx 0$, respecting $\delta\tau_p \gg \sigma_p$. Furthermore, the pulse widths σ_s, σ_i are assumed to be shorter than the dephasing times, but large enough to concentrate the pulses $\tilde{\boldsymbol{E}}_s(t)$ and $\tilde{\boldsymbol{E}}_i(t)$ respectively in infrared and ultraviolet frequencies such that they are respectively in resonance with intra manifold vibrational transitions and inter manifold vibronic transitions.

The final sum over states expression for the

classical signal is then given by,

$$\tilde{\mathcal{S}}^{(c)}(\bar{\omega}_p, \Omega_{si}) = \bar{C} I_p^{3/2} \sum_{n_\mathrm{e}} \frac{1}{\bar{\omega}_p - (\omega_{\mathrm{e}_{n_\mathrm{e}}} - \omega_{\mathrm{g}_1}) + i\gamma_{\mathrm{e}_{n_\mathrm{e}}\mathrm{g}_1}} \times \left(\sum_{n'_\mathrm{e}} \frac{\boldsymbol{\mu}_{\mathrm{e}_{n'_\mathrm{e}}\mathrm{e}_{n_\mathrm{e}}} \cdot \boldsymbol{\mu}_{\mathrm{g}_1\mathrm{e}_{n'_\mathrm{e}}} \times \boldsymbol{\mu}_{\mathrm{e}_{n_\mathrm{e}}\mathrm{g}_1}}{\Omega_{si} - (\omega_{\mathrm{e}_{n_\mathrm{e}}} - \omega_{\mathrm{e}_{n'_\mathrm{e}}}) + i\gamma_{\mathrm{e}_{n_\mathrm{e}}\mathrm{e}_{n'_\mathrm{e}}}} - \sum_{n_\mathrm{g}} \frac{\boldsymbol{\mu}_{\mathrm{g}_1\mathrm{g}_{n_\mathrm{g}}} \cdot \boldsymbol{\mu}_{\mathrm{g}_{n_\mathrm{g}}\mathrm{e}_{n_\mathrm{e}}} \times \boldsymbol{\mu}_{\mathrm{e}_{n_\mathrm{e}}\mathrm{g}_1}}{\Omega_{si} - (\omega_{\mathrm{g}_{n_\mathrm{g}}} - \omega_{\mathrm{g}_1}) + i\gamma_{\mathrm{g}_{n_\mathrm{g}}\mathrm{g}_1}} \right). \tag{11}$$

where we absorbed all the irrelevant constants into $\bar{C}$. Moreover, we have introduced phenomenological dephasing rates $\gamma_{\sigma_n\sigma'_{n'}}$. In the above equation, all the pulses are assumed to have the same intensity, I_p.

Quantum signals vs classical signals

Here, we provide few additional plots for the model system, presented in the main text, to show the advantage of the quantum signals. In Fig. (S2), the quantum and classical signals are plotted as a function of Ω_{si} with $\bar{\omega}_p$ chosen at the intermanifold vibronic resonances from the ground vibrational state of the ground manifold. Fig. (S2) clearly shows how $\tilde{\mathcal{S}}_0$ and $\tilde{\mathcal{S}}_1$ selectively isolate vibrational resonances, specifically at low frequencies in the region Ω_{si} $1000-1800\mathrm{cm}^{-1}$, which are buried under the shoulders in the classical signal, $\tilde{\mathcal{S}}^{(c)}$.

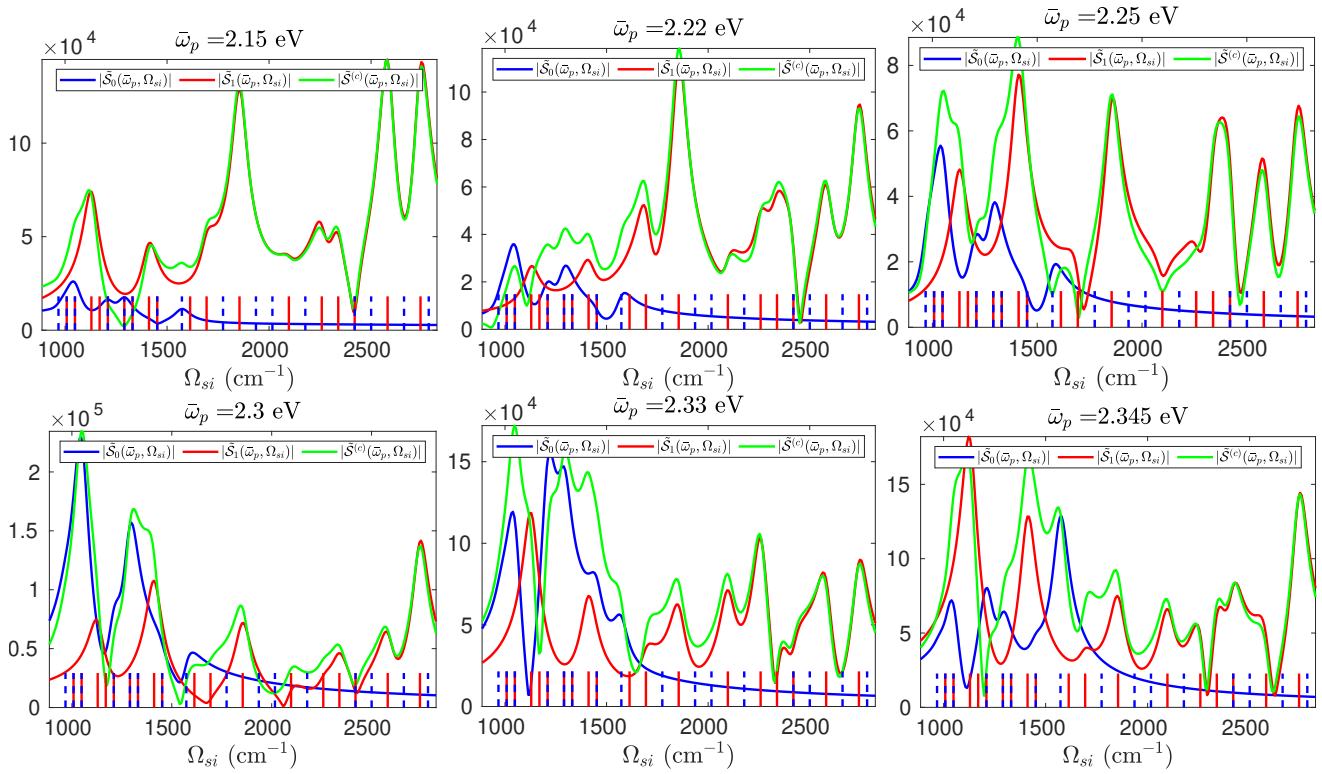

Figure S2: The quantum signals, $|\tilde{\mathcal{S}}_0|$ and $|\tilde{\mathcal{S}}_1|$ and the classical signal, $|\tilde{\mathcal{S}}^{(c)}|$ (their sum), are displayed as a function of Ω_{si} for fixed values of $\bar{\omega}_p$ (chosen at intermanifold vibronic resonances from the ground vibrational state of the ground manifold). Parameters used are same as for Fig. (5) of the main text. Red and dashed blue markers indicate allowed vibrational transitions in the ground and excited manifolds respectively.